coatings

MDPI

Article

ZnO Deposition on Silicon and Porous Silicon Substrate via Radio Frequency Magnetron Sputtering

Francisco Morales-Morales [1], Lizeth Martínez-Ayala [2,*], María R. Jiménez-Vivanco [3] and Heberto Gómez-Pozos [4]

[1] Optical Research Center, A. C., Loma del Bosque 115, Col. Lomas del Campestre, León 37150, Mexico; fcomm@cio.mx
[2] Tepeji Graduate School, Industrial Engineering, Autonomous Hidalgo State University, Av. Del Maestro No 41, Col. Noxtongo 2da Sección, Tepeji del Río de Ocampo 42855, Mexico
[3] Institute of Physics, UNAM, Circuito de la Investigación Científica, Ciudad Universitaria, México City 04510, Mexico; rayojimenezv@fisica.unam.mx
[4] Computing and Electronics Academic Area, ICBI, Autonomous Hidalgo State University, Carretera Pachuca/Tulancingo Km. 4.5, Pachuca 42184, Mexico; gpozos@uaeh.edu.mx
* Correspondence: lizeth_martinez@uaeh.edu.mx

Abstract: Nanostructured Zinc Oxide (ZnO) was deposited on silicon (c-Si) and macroporous silicon (m-PS) using a radio frequency (RF) reactive magnetron sputtering technique. Two RF powers of 60 and 80 W were selected for ZnO deposition on the substrates. Furthermore, the c-Si and m-PS substrate temperatures were kept at 500 and 800 °C, respectively. The morphological, structural, and optical characteristics of the samples were studied using scanning electron microscopy (SEM), an X-ray diffractometer (XRD), X-ray photoelectron spectroscopy (XPS), and photoluminescence spectroscopy (PL). The SEM images revealed the formation of ZnO nanorods on the c-Si and ZnO nanostructures constituted by the assembly of nanorods. It has been found that the increasing RF sputtering power caused the rise in the residual stress. In addition, the increase in the deposition temperature caused an improvement in the arrangement of the crystals, which was attributed to the decrease in crystal defects.

Keywords: zinc oxide; macroporous silicon; RF sputtering; structure; morphology properties

Citation: Morales-Morales, F.; Martínez-Ayala, L.; Jiménez-Vivanco, M.R.; Gómez-Pozos, H. ZnO Deposition on Silicon and Porous Silicon Substrate via Radio Frequency Magnetron Sputtering. *Coatings* **2023**, *13*, 1839. https://doi.org/10.3390/coatings13111839

Academic Editor: Alexander Tolstoguzov

Received: 31 August 2023
Revised: 17 October 2023
Accepted: 25 October 2023
Published: 27 October 2023

1. Introduction

ZnO is a semiconductor material with a wide band gap of 3.37 eV and a high excitation binding energy of 60 meV. In comparison to other semiconductor materials, ZnO has the main characteristics of presenting piezoelectricity, thermal and chemical stability, and high stability against environmental corrosions. It is also non-toxic, and its fabrication is low-cost [1–3]. Such properties have made ZnO an attractive material in technological applications, especially in light-emitting diodes [4,5], solar cells [6,7], catalysis [8–10], gas sensors [11–13], and optoelectronic devices [14,15]. ZnO applications become even more interesting when it is deposited on porous nanostructure substrates such as porous silicon (PS).

Recent studies on ZnO deposited on PS via EBIC (electron-beam-induced current) have demonstrated that ZnO/PS is an isotype heterojunction with the possibility of enhancing charge carrier flow, which makes it possible to obtain light-emitting diodes and solar cells [15]. Additionally, a sensor based on ZnO/PSNW (zinc oxide on porous silicon nanowires) showed excellent gas sensing performance for various NO_2 concentrations (5–50 ppm), reaching a high electrical resistance rate of 35% for 50 ppm of NO_2 [16]. Furthermore, studies revealed a pyroelectric coefficient in ZnO/PS 40 times higher than in ZnO/c-Si and a pyroelectric voltage as high as 2.4 V [17].

Various techniques have been applied to deposit ZnO on PS, such as spray pyrolysis [18,19], chemical vapor deposition [20], hydrothermal [3,21], sol–gel [22], and magnetron

sputtering [23]. There even exist computational methods to describe and understand the formation of ZnO, such as density functional theory (DFT) and ab initio molecular dynamics simulation (AIMD) [24,25].

In the present work, we applied the magnetron sputtering technique because is the most used and studied for its efficiency, high interfacial adhesion, and ability to deposit high-density films. Furthermore, magnetron sputtering allows thin films to be deposited on different types of substrates at high temperatures with excellent uniformity and quality crystallinity. From a practical point of view, the study of the properties of thin films at higher temperatures makes it possible to ensure the durability and repeatability of devices operated at high temperatures. Therefore, a material needs to exhibit good thermal stability at operating temperatures. In general, the thermal stability of a material depends on factors such as structural phases and the degree of crystallinity, which are correlated with the route of synthesis [26].

When the magnetron sputtering technique is adopted, the pressure, gas type, gas flow, temperature, and power deposition have a significant effect on the quality of the formed films. For example, the working pressure can change the grain size and crystal structure of deposited ZnO, allowing the films of deposited ZnO to be oriented in different crystalline planes. Likewise, deposits made with low power density show a very smooth surface and preferential orientation of the grains [27]. Furthermore, the increase in oxygen content in the argon environment results in a decrease in the deposition rate of the films [27]. Husam S. Al-Salam and M. J. Abdullah deposited ZnO on PS, maintaining an RF power deposition of 150 W with its posterior annealing at 500 °C during 2 h. The results revealed a high and deep porosity with a roughness of 178 nm [28]. K. Cicek et al. formed ZnO on PS and silicon utilizing the RF&DC magnetron sputtering technique with a flow rate of Ar and O_2 at 120 W power. They found that a pyroelectric coefficient of 8.2 can be achieved for deposits on PS, which is more than ~40 times higher than the one on Si substrate [17].

Although the deposition of ZnO films on PS substrates using the magnetron sputtering technique has been carried out, there are few reports detailing the study of higher temperatures and its comparison with power deposition on the properties of ZnO on PS. Under this scenario, it is of vital importance to study the synthesis parameters for the design and development of new devices. In this work, we have deposited ZnO on macroporous silicon using the magnetron sputtering technique, varying the RF power and the deposition temperature to study the effect caused by the porous substrate on the ZnO.

2. Materials and Methods

Macroporous Silicon (m-PS) substrates were fabricated on p-type crystalline Silicon (c-Si) wafers with a thickness of about 280 µm. The typical resistivity was 5–10 Ωcm and the planar orientation was (100). The native surface oxide on the reference wafers was chemically etched with a hydrofluoric acid solution (HF). Later, m-PS substrates were obtained via the electrochemical etching of c-Si, with a density current of 4 mA/cm^2 for 15 min, using a mixture of hydrofluoric acid (HF, 48 wt.%) and dimetylformamide ($HCON(CH_3)_2$, 99.9 wt.%) as an electrolyte in the volumetric ratio of 1:3. Finally, m-PS substrates were oxidized for 30 min in the air to stabilize their surface [8–10,13]. ZnO film deposition on m-PS was achieved through magnetron sputtering (ATC Orion 8 Cluster Flange, Aja International, Hingham, MA, USA.) using two radio frequency (RF) powers of 60 W (A) and 80 W (B), respectively. It is important to note that in each deposition of ZnO, the temperature of the substrates was kept at 500 °C (A5/m-PS, B5/m-PS) and 800 °C (A8/m-PS, B8/m-PS) for 1 h. The deposition was achieved using a 2-inch ZnO target with 99.99% purity, the base pressure of the system was 2×10^{-6} Torr, and the Ar flow was 30 sccm, to obtain a working pressure of 5×10^{-3} Torr. The ZnO films were deposited on c-Si to obtain the reference samples: A5/c-Si, A8/c-Si, B5/c-Si, and B8/c-Si. Table 1 shows the summary of the prepared samples. The surface morphology of the fabricated structures was characterized using a scanning electron microscope (SEM, JEOL JSM-7800F, Tokyo, Japan). The ZnO crystal structures were studied using an X-ray diffractometer (XRD,

ORION, D2 PHASER Bruker, Baden-Wurtemberg, Karlsrueh, Germany) using the CuK_α radiation and λ = 0.15406 nm. An X-ray photoelectron spectroscope (XPS, Thermo K-Alpha, Waltham, MA, USA) equipped with an Al Kα monochromatic X-ray source (*hv* = 1486.6 eV) in an analysis chamber at a base pressure of 10^{-7} mbar was used to investigate the chemical state of the elements in the prepared ZnO. Photoluminescence studies were carried out using a Varian fluorescence spectrometer (Cary Eclipse, Varian Inc., Palo Alto, CA, USA) under 325 nm excitation.

Table 1. Summary of samples fabricated.

Sample	Substrate	Temperature (°C)	RF Power (W)
A5/c-Si	silicon	500	60
B5/c-Si			80
A8/c-Si		800	60
B8/c-Si			80
A5/m-PS	macroporous silicon	500	60
B5/m-PS			80
A8/m-PS		800	60
B8/m-PS			80

3. Results

3.1. Scanning Electronic Microscopy (SEM)

SEM micrographs were obtained to study the effects of RF power and temperature during the deposition of ZnO on the substrates. Figure 1 shows the top-view and cross-sectional SEM images of m-PS substrates with interconnected pores. These pores had a diameter between 100 and 200 nm and a thickness around 200 nm.

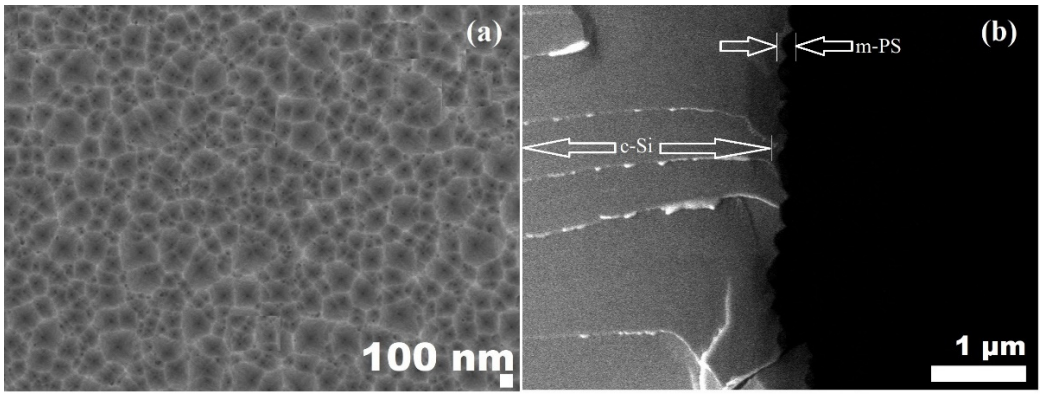

Figure 1. SEM image of top view (**a**) and cross-section (**b**) of bare m-PS substrates.

Figure 2 shows SEM micrographs of ZnO deposited on c-Si and m-PS after the RF sputtering process. We can observe that ZnO film fully covers the m-PS substrate (Figure 2b,d,f,h). One may also note that the ZnO samples growth at 500 °C (Figure 2a–d) was characterized by continuous and dense ZnO agglomerates. These agglomerates were distributed uniformly on the substrates, indicating that the ZnO deposit does not have a well-defined structure. On the other hand, the SEM images of samples deposited at 800 °C (Figure 2e–h) revealed the formation of better-defined nanostructures. This could be because, with the increase in deposition temperature, coalescence is enhanced and atomic mobility increases, causing the formation of better-defined structures [29,30].

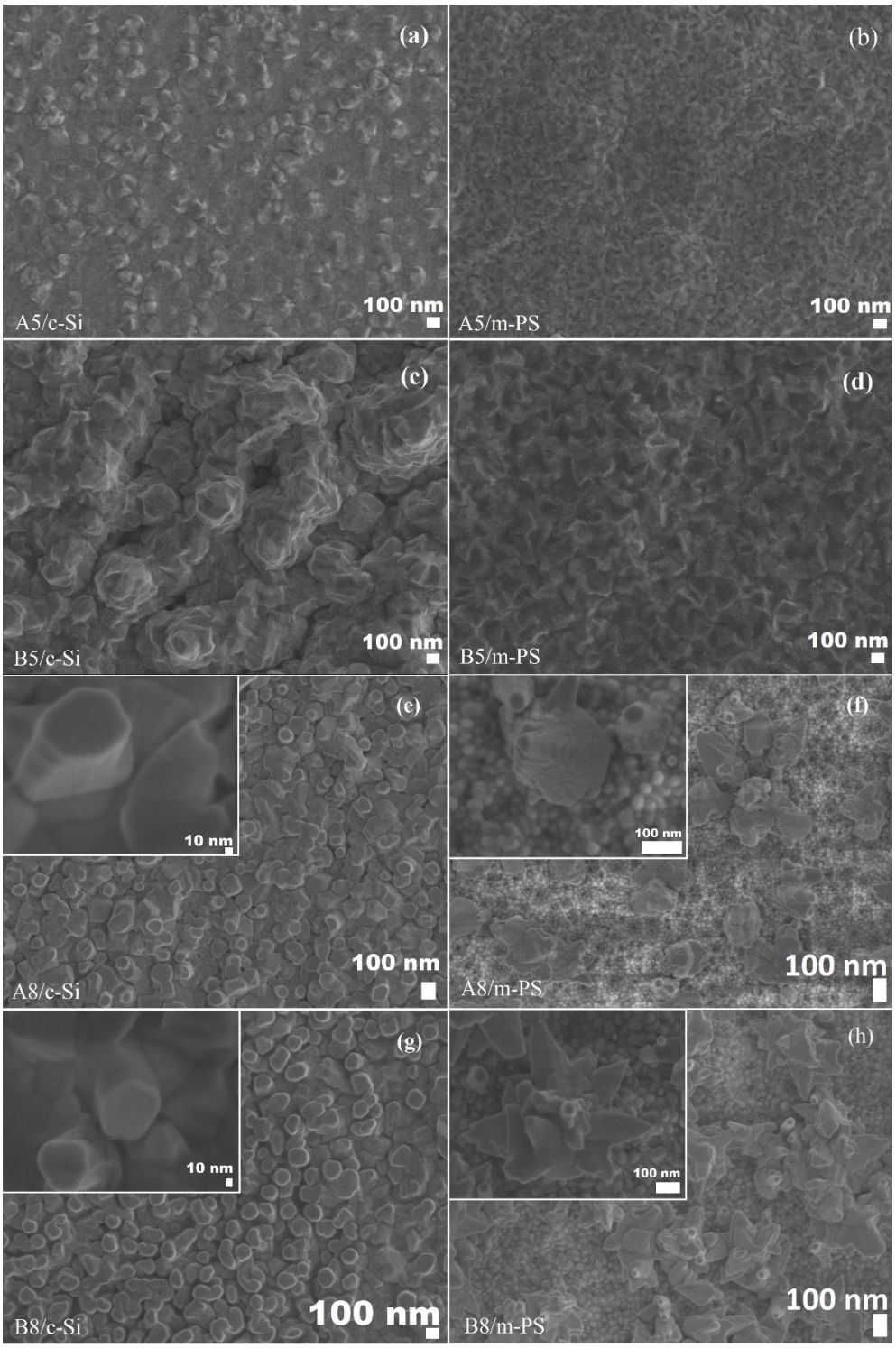

Figure 2. SEM images of ZnO deposited on c-Si (left images) and m-PS (right images) at RF power of 60 W (**a**,**b**,**e**,**f**) and 80 W (**c**,**d**,**g**,**h**) for different temperature deposition: 500 °C (**a**–**d**) and 800 °C (**e**–**h**).

Figure 2e,g indicate the formation of ZnO nanorods on the c-Si substrates. The samples with ZnO deposited on m-PS (Figure 2f,h) revealed the formation of ZnO nanostructures constituted by the assembly of nanorods. Likewise, it can be observed that such nanostructures were grown over smaller nanoparticles with diameter sizes around 29 and 35 nm for the samples A8/m-PS and B8/m-PS, respectively (inside Figure 2f,h). Unlike ZnO grown on c-Si substrates, ZnO growth on m-PS acquires enough activation energy to occupy the

correct nuclei-sites along the porous surface; thus, grains with lower surface energy tend to grow [31]. Additionally, with increasing RF power, Zn and O atoms do not have enough time to diffuse to their optimal sites in the porous substrates, causing the formation of tilted grains (Figure 2f,h) [29,30,32]. With the rise in RF power deposition from 60 to 80 W, the growth rate rises, which results in an increase in the amount of ZnO nanostructures on the substrates (Figure 2g,h). The tiny particles below the ZnO nanostructures could be on the substrate surface due to the confinement effect of the nanostructured matrix of the m-PS substrate [33].

3.2. X-ray Diffraction (XRD)

The crystal structure of our samples was investigated through X-ray diffraction spectroscopy (XRD). The diffractograms obtained from the ZnO/c-Si and ZnO/m-PS samples as a function of RF sputtering deposition power (60 and 80 W) and temperature (500 and 800 °C) are shown in Figure 3. The characteristic peak corresponds to the reflection (002) plane in ZnO/c-Si, indicating a single crystalline wurtzite phase with a preferential orientation towards the c-axis. The c-axis indicates that the ZnO growth is perpendicular to the substrate surface (Figure 3a).

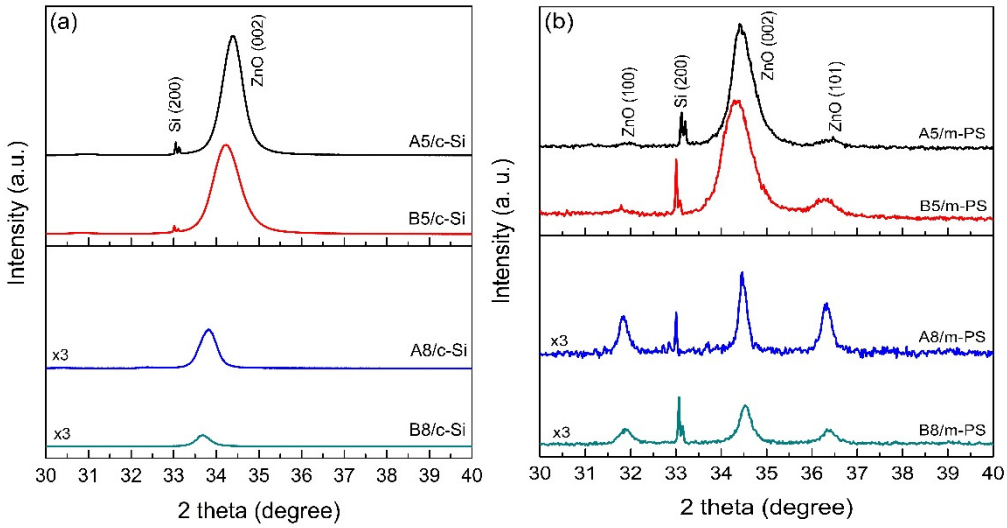

Figure 3. X-ray diffraction spectra for the ZnO deposited on c-Si (**a**) and m-PS (**b**) at different temperatures and power deposition via RF magnetron sputtering.

On the other hand, various diffraction peaks were observed in the ZnO deposited on m-PS (Figure 3b) around 31.87°, 34.51°, and 36.35°, corresponding to the (100), (002), and (101) planes, respectively. The above indicates that the samples with ZnO deposited on m-PS are polycrystalline and have a hexagonal wurtzite structure (JCPDS No. 36-1451). The ZnO (002) orientation has been attributed to the lowest surface free energy provided by the m-PS substrates, which induces ZnO growth perpendicular to the surface [34]. At the same, all diffractograms show a peak in the plane (200), indicating the presence of silicon in the substrates [35].

The XRD measurements allowed us to evaluate the crystalline size (D), density dislocation (δ), biaxial stress (σ), and d-spacing (d). The D of ZnO/m-PS samples was calculated using the Debye Scherrer formula, while δ, σ, and d were calculated using the following formulas [31,36]:

$$\delta = \frac{1}{D^2} \tag{1}$$

$$\sigma = -453.6 \times 10^9 \left[\frac{c - c_0}{c_0} \right] \tag{2}$$

$$d = \frac{\lambda}{2\sin\theta} \quad (3)$$

where c is the lattice parameter of the strained ZnO calculated from X-ray diffraction data, and c_0 is the strain-free lattice parameter (c_0 = 0.5206 nm) (JCPDS 36-1451). All the diffraction peaks, crystallite size, and respective d-spacing values are tabulated in Table 2. From Table 2, we can observe good agreement with the standard values. It can also show a % d error, and it has been observed that the difference between experimental and standard values is within the acceptable range. Table 3 shows the full width half maximum (FWHM), D, δ, and σ obtained for the (002) orientation in the samples.

Table 2. The X-ray diffraction peaks, 2θ, d-spacing, % d error, crystal size, and average crystal size of ZnO deposited on c-Si and m-PS.

Sample	(hkl)	2θ JCPDS	2θ Experimental	d-Spacing JCPDS	d-Spacing Experimental	% d Error	*D* (nm)	Average *D* (nm)
A5/c-Si	(002)	34.4937	34.4044	2.60332	2.605	0.05	15.01	15
B5/c-Si	(002)	34.4937	34.2269	2.60332	2.618	0.55	11.72	12
A8/c-Si	(002)	34.4937	33.8357	2.60332	2.647	1.68	18.42	18
B8/c-Si	(002)	34.4937	33.7026	2.60332	2.657	2.07	22.24	22
A5/m-PS	(002)	34.4937	34.4700	2.60332	2.600	0.14	13.76	17
	(101)	36.4084	36.3904	2.47592	2.467	0.36	19.32	
B5/m-PS	(002)	34.4937	34.4783	2.60332	2.599	0.16	11.19	15
	(101)	36.4084	36.2574	2.47592	2.476	0.01	17.89	
A8/m-PS	(100)	31.8384	31.8459	2.81430	2.808	0.23	33.65	33
	(002)	34.4937	34.3530	2.60332	2.608	0.19	36.15	
	(101)	36.4084	36.2755	2.47592	2.474	0.06	29.21	
B8/m-PS	(100)	31.8384	31.8932	2.81430	2.804	0.38	25.04	24
	(002)	34.4937	34.5327	2.60332	2.595	0.31	23.63	
	(101)	36.4084	36.3742	2.47592	2.468	0.32	22.55	

Table 3. FWHM, crystallite size, dislocation density, and biaxial stress of ZnO deposited on c-Si and m-PS via RF magnetron sputtering.

Sample	2θ (°)	FWHM	*D* (nm)	δ (1/nm^2)	σ (Gpa)
A5/c-Si	34.4044	0.5544	15	0.0044	−1.2631
B5/c-Si	34.2269	0.7094	12	0.0073	−0.9764
A8/c-Si	33.8357	0.4508	18	0.0029	−1.5607
B8/c-Si	33.7026	0.3732	22	0.002	−1.8944
A5/m-PS	34.4151	0.5572	15	0.0045	−1.2561
B5/m-PS	34.3264	0.963	9	0.0134	−0.7075
A8/m-PS	34.4946	0.2054	41	0.0006	−3.486
B8/m-PS	34.5317	0.3015	28	0.0013	−2.3607

According to Table 3 (from 500 to 800 °C), the broadening of FWHM decreased due to the temperature increase. This could be attributed to the fact that with the rise of temperature, atom diffusion (Zn and O) in the crystal's arrangement increases, causing enhanced crystallinity. Haiyan Wang et al. demonstrated via XPS and photoluminescence analysis that the increase in annealing temperature (from 600 to 900 °C) provides a great force for O atoms to diffuse into ZnO thin films. This reduces the number of oxygen vacancies/defects and defects of Zn [37]. The enhancement in crystallinity can be corroborated with the diminution in δ values. The dislocation density represents the irregularities and the number of crystalline defects in the crystal as oxygen and zinc interstitials [38,39]. It is also observed that with the increased RF power deposition, the atoms receive more energy and have more driving force. This leads to an increase in intrinsic stress, as evidenced by the increase in residual stress on the ZnO lattice. Such intrinsic stress is due to the accumulating effect of the crystallographic flaws during deposition (increase of δ values) [38,40]. From Table 3, it can also be observed that residual stress decreases for samples A5/c-Si and

B8/c-Si. This may be due to the mechanical instability of ZnO nanorods. M. Riaz et al. reported the relationship between the pore diameter of nanorods and residual stress [41]. They found that with the increase in pore diameter, the residual stress tends to increase. The above is reflected in the shift of the angle towards higher angles.

3.3. X-ray Photoelectron Spectroscopy (XPS)

The oxidation state of ZnO on c-Si and m-PS via RF sputtered at different temperatures and deposition powers was investigated using XPS (Figure 4). Figure 4a,b show the characteristics peaks assigned to zinc (Zn), oxygen (O), and carbon (C). Figure 4c,d show high-resolution spectra of the Zn 2p region for the samples. It can be observed that the $Zn2p_{3/2}$ core levels are located at around 1022.00 and 1022.05 eV for ZnO deposited on c-Si and m-PS, respectively, while the $Zn2p_{1/2}$ core levels are located at around 1045.13 and 1045.05 eV for ZnO deposited on c-Si and m-PS, respectively. The core level from $Zn2p_{3/2}$ has been assigned to the Zn^{2+} ions in the ZnO thin films [42]. It can be seen that the position of the peaks differs slightly; this is probably because of the different surface morphologies of the deposited ZnO [43].

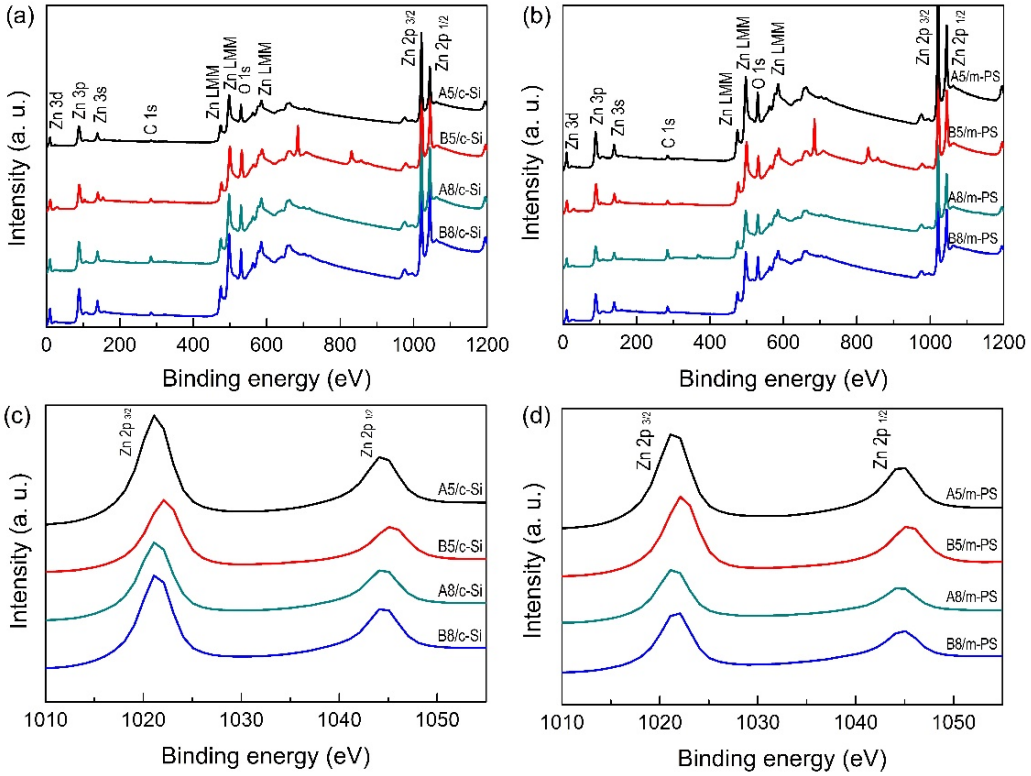

Figure 4. XPS spectra (**a**,**b**) and high-resolution spectra of Zn 2p (**c**,**d**) for the ZnO deposited on c-Si (left spectra) and m-PS (right spectra) via RF magnetron sputtering technique at different temperatures and power deposition.

The high-resolution spectra and deconvolution of the O1s peak were obtained to further study the binding state of Zn and O. The deconvolution of the XPS peaks was performed using Fityk software (1.3.1 version). Figure 5 shows the O1s scan spectra of ZnO deposited on c-Si and m-PS at different temperatures and power depositions. Three peaks were observed around 527.62 eV (1), 530.54 eV (2), and 533.34 eV (3). The peak (1) is characteristic of the metal oxides [44]. The peak (2), at a low binding energy, is associated with O^{2-} ions in the deficient regions within the ZnO array [45]. It can also be associated with hydrated oxides that could have been incorporated from the deposition chamber or the presence of weakly bound oxygen on the surface of the films [45]. Weijia Yang et al. attributed binding energy of around 530.75 eV to oxygen defects/vacancies. The central

level of peak (2) shows asymmetry, indicating the presence of various forms of oxygen bonds in the near-surface region of ZnO [46]. The intensity is associated with the number of oxygen vacancies [42,47]. The peak (3) is associated with hydroxyl groups (–OH), O^2, or C–O bonds of chemisorbed or adsorbed species on the sample surface [43,47,48]. Previously, it has been reported that intrinsic defects, such as zinc interstitial atoms (Zn_i) and oxygen vacancies (V_O), are electrically active and can induce localized states near the conduction band. These species can act as donors [48].

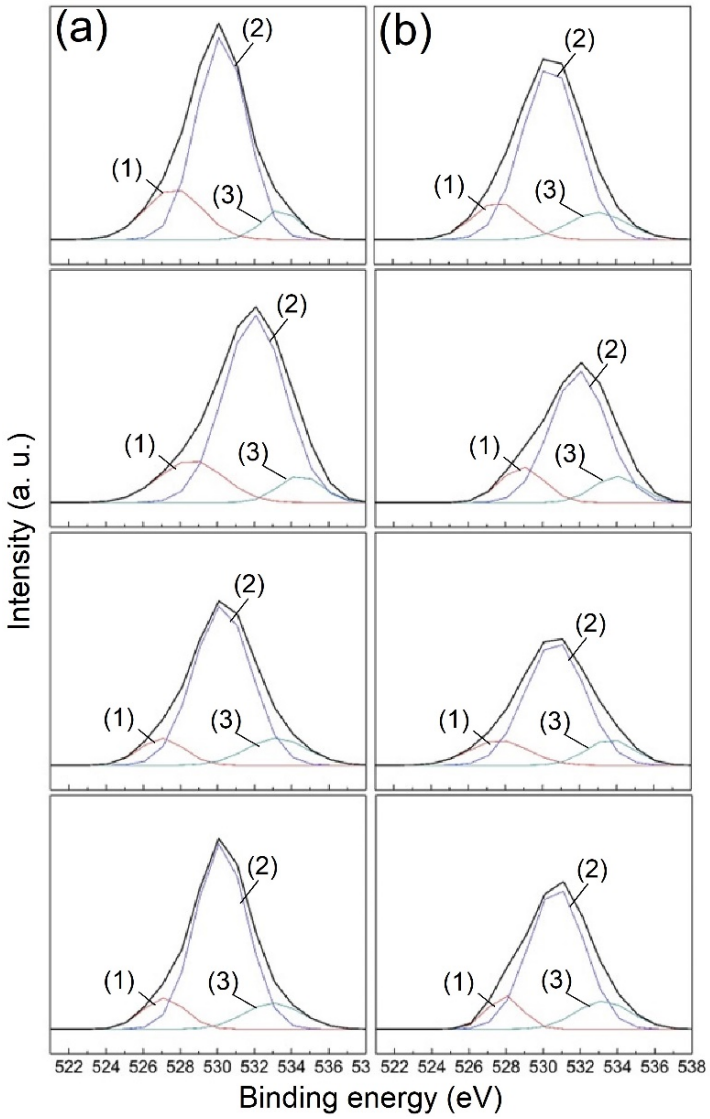

Figure 5. High-resolution and deconvolution of the O1s scan spectra of ZnO deposited on c-Si (**a**) and m-PS (**b**) at different temperatures and power deposition via RF magnetron sputtering.

3.4. Photoluminescence (PL)

Photoluminescence (PL) is a very sensitive characterization technique that helps to identify the crystallinity and defects present in ZnO. The spectra and bandgap transition schematic of the ZnO/m-PS samples are shown in Figure 6. ZnO PL emission spectra are composed of the near-band-edge (NBE) in the UV region, which is considered a characteristic emission of ZnO [49], and the deep-level-emission region (DL) in the visible region, which is universally associated with native defects in ZnO. The emission peak at ~360 nm is primarily related to the free exciton transition in the NBE. In contrast, the multiple jumps from DL emission are attributed to the photogenerated hole recombination on the ZnO structural defects [50,51]. On the other hand, violet emission in the 388–440 nm range is

mainly referred to by the Zn interstitials found in the space charge region near the surface [52–54]. Furthermore, blue-green emission placed at 520 nm is commonly associated with the oxygen vacancies (V_{Zn}) [53,55,56], and 545 nm emission is attributed to the oxygen vacancies (V_o) [50,54]. Yellow emission in 595 nm and orange in 643–648 nm are related to oxygen anti-sites [54,57]. Finally, red emission at 720–724 nm is due to (V_o) [58,59].

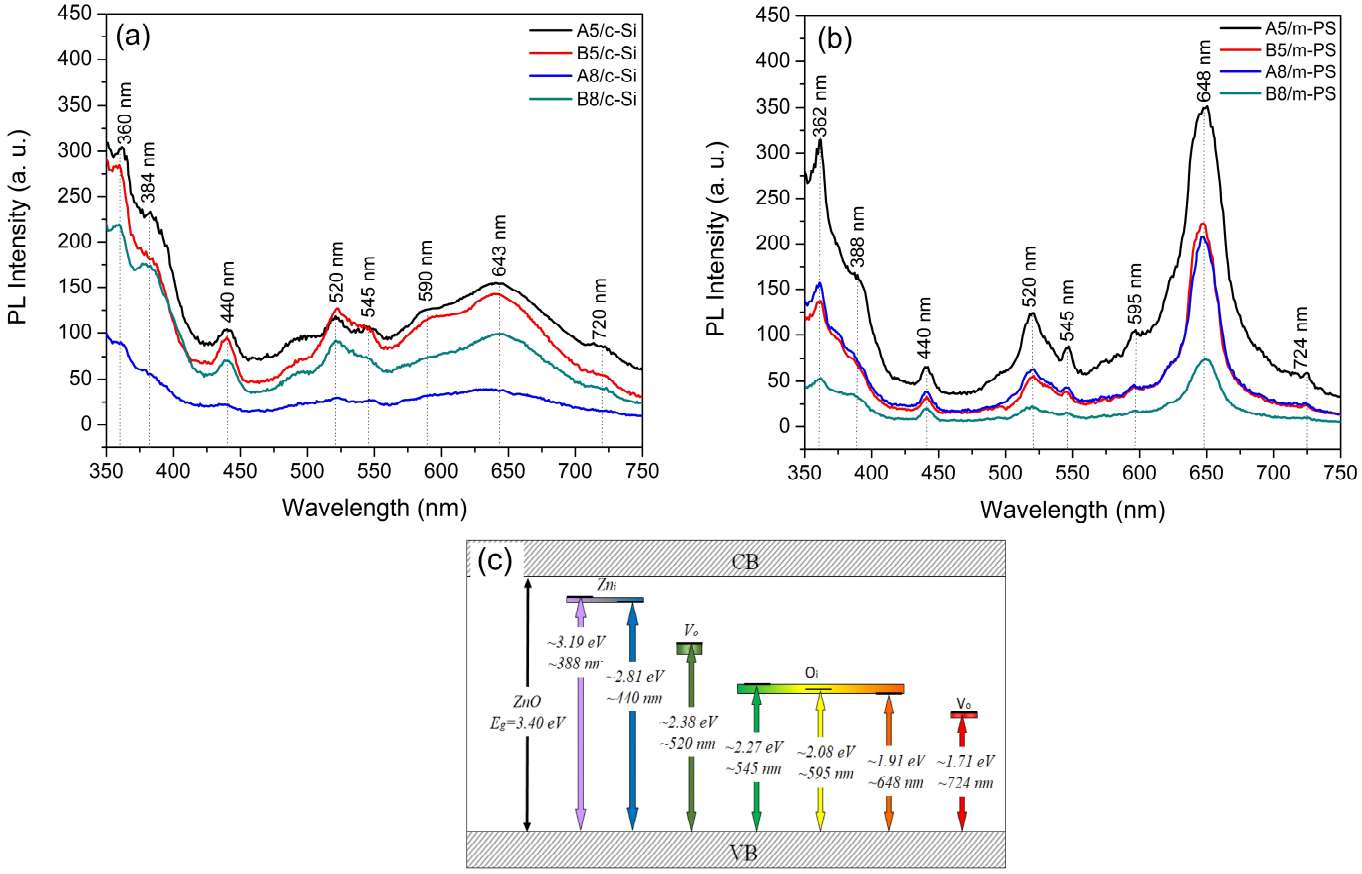

Figure 6. Photoluminescence spectra of ZnO/c-Si (**a**) and ZnO/m-PS (**b**) samples. The lower subfigure shows the schematic bandgap diagram (**c**).

As is shown in the previous figure, there is no shift in the peak position during RF power and temperature variation. However, a significant change in peak emission intensity is observed. The peak intensity is reduced as the deposition temperature increases. This phenomenon may indicate that there is a Zn and O defect decrease on the m-PS substrate, as can be noted in Table 3. In a similar way, the peak emission is affected inversely by the RF power. An increment in the RF power causes a reduction in the peak emission intensity, which is attributed to the crystallinity reduction in the samples, as indicated in the XRD results [51,59].

4. Conclusions

ZnO was successfully deposited over c-Si and m-PS using the reactive RF magnetron sputtering method. The formation of ZnO nanorods on the c-Si and ZnO nanostructures constituted by nanorod assembly on m-PS was revealed. Increased RF energy deposition results in an increase in ZnO nanostructures on the substrates and a rise in residual stress. All the ZnO nanostructures show evident (002)-preferred orientation, corresponding to the wurtzite structure. On the other hand, the increase in deposition temperature caused an improvement in the arrangement of the crystals, which was attributed to the decrease in crystal defects. XPS and PL results confirm the presence of ZnO structural defects, which can conduce the fabrication of sensors and gas devices.

Author Contributions: Conceptualization, data curation, formal analysis, and investigation, L.M.-A. and F.M.-M.; methodology and project administration, L.M.-A.; resources, F.M.-M.; visualization and supervision, M.R.J.-V.; validation, writing—review and editing, M.R.J.-V. and H.G.-P. All authors have read and agreed to the published version of the manuscript.

Funding: This research received no external funding.

Institutional Review Board Statement: Not applicable.

Informed Consent Statement: Not applicable.

Data Availability Statement: Not applicable.

Acknowledgments: The authors are grateful to Vivechana Agarwal and Y. Kumar (CIICAp-UAEM) and CINVESTAV-IPN for help with PL and XPS measurements, respectively.

Conflicts of Interest: The authors declare no conflict of interest.

References

1. Li, C.-F.; Hsu, C.-Y.; Li, Y.-Y. NH_3 sensing properties of ZnO thin films prepared via sol–gel method. *J. Alloys Compd.* **2014**, *606*, 27–31. [CrossRef]
2. Daryakenari, A.A.; Daryakenari, M.A.; Bahari, Y.; Omivar, H. Preparation and Ethanol Sensing Properties of ZnO Nanoparticles via a Novel Sol-Gel Method. *ISRN Nanotechnol.* **2012**, *2012*, 879480. [CrossRef]
3. Zviagin, A.S.; Chernozem, R.V.; Surmeneva, M.A.; Pyeon, M.; Frank, M.; Ludwig, T.; Tutacz, P.; Ivanov, Y.F.; Mathur, S.; Surmenev, R.A. Enhanced piezoelectric response of hybrid biodegradable 3D poly(3-hydroxybutyrate) scaffolds coated with hydrothermally deposited ZnO for biomedical applications. *Eur. Polym. J.* **2019**, *117*, 272–279. [CrossRef]
4. Rahman, F. Zinc oxide light-emitting diodes: A review. *Opt. Eng.* **2019**, *58*, 010901. [CrossRef]
5. Moyen, E.; Kim, J.H.; Kim, J.; Jang, J. ZnO Nanoparticles for Quantum-Dot-Based Light-Emitting Diodes. *ACS Appl. Nano Mater.* **2020**, *3*, 5203–5211. [CrossRef]
6. Rodríguez-Guadarrama, L.A.; Alonso-Lemus, I.L.; Escorcia-García, J. Emerging coaxial nanostructures for clean energy generation and storage systems: A minireview. *J. Mater. Res.* **2021**, *36*, 4084–4101. [CrossRef]
7. Javed, A.H.; Shahzad, N.; Khan, M.A.; Ayub, M.; Iqbal, N.; Hassan, M.; Hussain, N.; Rameel, M.I.; Shahzad, M.I. Effect of ZnO nanostructures on the performance of dye sensitized solar cells. *Sol. Energy* **2021**, *230*, 492–500. [CrossRef]
8. Huh, J.; Park, J.; Kim, G.T.; Park, J.Y. Highly sensitive hydrogen detection of catalyst-free ZnO nanorod networks suspended by lithography-assisted growth. *Nanotechnology* **2011**, *22*, 085502. [CrossRef]
9. Gao, L.; Nefzaoui, E.; Marty, F.; Erfan, M.; Bastide, S.; Leprince-Wang, Y.; Bourouina, T. TiO_2-Coated ZnO Nanowire Arrays: A Photocatalyst with Enhanced Chemical Corrosion Resistance. *Catalysts* **2021**, *11*, 1289. [CrossRef]
10. Tran, S.B.T.; Choi, H.S.; Oh, S.Y.; Moon, S.Y.; Park, J.Y. Iron-doped ZnO as a support for Pt-based catalysts to improve activity and stability: Enhancement of metal–support interaction by the doping effect. *RSC Adv.* **2018**, *8*, 21528–21533. [CrossRef]
11. Franco, M.A.; Conti, P.P.; Andre, R.S.; Correa, D.S. A review on chemiresistive ZnO gas sensors. *Sensors Actuators Rep.* **2022**, *4*, 100100. [CrossRef]
12. Ananthi, S.; Kavitha, M.; Kumar, E.R.; Prakash, T.; Poonguzhali, R.V.; Ranjithkumar, B.; Balamurugan, A.; Srinivas, C.; Sastry, D. Investigation of physicochemical properties of ZnO nanoparticles for gas sensor applications. *Inorg. Chem. Commun.* **2022**, *146*, 110152. [CrossRef]
13. Guo, J.; Zhang, J.; Zhu, M.; Ju, D.; Xu, H.; Cao, B. High-performance gas sensor based on ZnO nanowires functionalized by Au nanoparticles. *Sensors Actuators B Chem.* **2014**, *199*, 339–345. [CrossRef]
14. Abed, A.L.; Khalef, W.K.; Salim, E.T. Synthesis, Characterization and Optoelectronic device application of ZnO nano structure. *J. Phys. Conf. Ser.* **2021**, *1795*, 012031. [CrossRef]
15. Morales–Morales, F.; Benítez-Lara, A.; Hernández-Sebastián, N.; Ambriz-Vargas, F.; Jiménez-Vivanco, M.; López, R.; Morales–Sánchez, A. Study of zinc oxide/porous silicon interface for optoelectronic devices. *Mater. Sci. Semicond. Process.* **2022**, *148*, 106810. [CrossRef]
16. Liao, J.; Li, Z.; Wang, G.; Chen, C.; Lv, S.; Li, M. ZnO nanorod/porous silicon nanowire hybrid structures as highly-sensitive NO_2 gas sensors at room temperature. *Phys. Chem. Chem. Phys.* **2016**, *18*, 4835–4841. [CrossRef]
17. Cicek, K.; Karacali, T.; Efeoglu, H.; Cakmak, B. Deposition of ZnO thin films by RF&DC magnetron sputtering on silicon and porous-silicon substrates for pyroelectric applications. *Sensors Actuators A Phys.* **2017**, *260*, 24–28. [CrossRef]
18. Mata, V.; Maldonado, A.; Olvera, M.d.l.L. Deposition of ZnO thin films by ultrasonic spray pyrolysis technique. Effect of the milling speed and time and its application in photocatalysis. *Mater. Sci. Semicond. Process.* **2018**, *75*, 288–295. [CrossRef]
19. Vista de Síntesis de Nanohojuelas de ZnO Mediante la Técnica Rocío Químico por Ultrasonicación. Available online: https://repository.uaeh.edu.mx/revistas/index.php/tepexi/article/view/6558/7736 (accessed on 4 July 2023).
20. Gutiérrez, D.R.; García-Salgado, G.; Coyopol, A.; Rosendo-Andrés, E.; Romano, R.; Morales, C.; Benítez, A.; Severiano, F.; Herrera, A.M.; Ramírez-González, F. Effect of the Deposit Temperature of ZnO Doped with Ni by HFCVD. *Materials* **2023**, *16*, 1526. [CrossRef]

21. Edalati, K.; Shakiba, A.; Vahdati-Khaki, J.; Zebarjad, S.M. Low-temperature hydrothermal synthesis of ZnO nanorods: Effects of zinc salt concentration, various solvents and alkaline mineralizers. *Mater. Res. Bull.* **2016**, *74*, 374–379. [CrossRef]
22. Manikandan, B.; Endo, T.; Kaneko, S.; Murali, K.R.; John, R. Properties of sol gel synthesized ZnO nanoparticles. *J. Mater. Sci. Mater. Electron.* **2018**, *29*, 9474–9485. [CrossRef]
23. Abdallah, B.; Jazmati, A.K.; Refaai, R. Oxygen Effect on Structural and Optical Properties of ZnO Thin Films Deposited by RF Magnetron Sputtering. *Mater. Res.* **2017**, *20*, 607–612. [CrossRef]
24. Filho, M.A.M.; Hsiao, C.-L.; dos Santos, R.B.; Hultman, L.; Birch, J.; Gueorguiev, G.K. Self-Induced Core–Shell InAlN Nanorods: Formation and Stability Unraveled by Ab Initio Simulations. *ACS Nanosci. Au* **2023**, *3*, 84–93. [CrossRef] [PubMed]
25. Lundgren, C.; Kakanakova-Georgieva, A.; Gueorguiev, G.K. A perspective on thermal stability and mechanical properties of 2D Indium Bismide from ab initio molecular dynamics. *Nanotechnology* **2022**, *33*, 335706. [CrossRef] [PubMed]
26. Vu, T.H.; Pham, A.T.; Nguyen, V.Q.; Nguyen, A.D.; Tran, T.N.N.; Thi, M.H.N.; Kim, Y.S.; Tran, V.T.; Cho, S. Growth and thermal stability studies of layered GaTe single crystals in inert atmospheres. *J. Solid State Chem.* **2021**, *296*, 121996. [CrossRef]
27. Damiani, L.R.; Mansano, R.D. Zinc oxide thin films deposited by magnetron sputtering with various oxygen/argon concentrations. *J. Phys. Conf. Ser.* **2012**, *370*, 012019. [CrossRef]
28. Al-Salman, H.S.; Abdullah, M. Preparation of ZnO nanostructures by RF-magnetron sputtering on thermally oxidized porous silicon substrate for VOC sensing application. *Measurement* **2015**, *59*, 248–257. [CrossRef]
29. Chen, Y.; Shih, Y.; Ho, C.; Du, J.; Fu, Y. Effect of temperature on lateral growth of ZnO grains grown by MOCVD. *Ceram. Int.* **2010**, *36*, 69–73. [CrossRef]
30. Shabannia, R. Effect of annealing temperature on the structural, optical and electrical properties of ZnO thin films grown chemically on PS substrate. *J. Mater. Sci. Mater. Electron.* **2016**, *27*, 6413–6418. [CrossRef]
31. Zhong, W.; Liu, F.; Cai, L.; Zhou, C.; Ding, P.; Zhang, H. Annealing effects of co-doping with Al and Sb on structure and optical–electrical properties of the ZnO thin films. *J. Alloys Compd.* **2010**, *499*, 265–268. [CrossRef]
32. Lu, Y.; Hwang, W.; Liu, W.; Yang, J. Effect of RF power on optical and electrical properties of ZnO thin film by magnetron sputtering. *Mater. Chem. Phys.* **2001**, *72*, 269–272. [CrossRef]
33. Balderas-Valadez, R.; Antúnez, E.; Olive-Méndez, S.; Pacholski, C.; Campos-Alvarez, J.; Bokhimi, X.; Agarwal, V. Porous silicon pillar and bilayer structure as a nucleation center for the formation of aligned vanadium pentoxide nanorods. *Ceram. Int.* **2017**, *43*, 8023–8030. [CrossRef]
34. Wang, Y.; Tang, W.; Zhang, L. Crystalline Size Effects on Texture Coefficient, Electrical and Optical Properties of Sputter-deposited Ga-doped ZnO Thin Films. *J. Mater. Sci. Technol.* **2015**, *31*, 175–181. [CrossRef]
35. Zaumseil, P. High-resolution characterization of the forbidden Si 200 and Si 222 reflections. *J. Appl. Crystallogr.* **2015**, *48*, 528–532. [CrossRef]
36. Martínez, L.; García-Salgado, G.; Morales-Morales, F.; Campillo, B.; Hernández, A.G.; Karthik, T.V.K.; Jiménez-Vivanco, M.R.; Campos-Álvarez, J. ZnO Films Incorporation Study on Macroporous Silicon Structure. *Materials* **2021**, *14*, 3697. [CrossRef]
37. Wang, H.; Tang, C.; Yang, W.; Zhao, J.; Liu, L.; Mu, J.; Zhang, Y.; Zeng, C. Recrystallization behavior, oxygen vacancy and photoluminescence performance of sputter-deposited Ga_2O_3 films via high-vacuum in situ annealing. *Ceram. Int.* **2022**, *48*, 3481–3488. [CrossRef]
38. Meriche, F.; Touam, T.; Chelouche, A.; Dehimi, M.; Solard, J.; Fischer, A.; Boudrioua, A.; Peng, L.-H. Post-annealing effects on the physical and optical waveguiding properties of RF sputtered ZnO thin films. *Electron. Mater. Lett.* **2015**, *11*, 862–870. [CrossRef]
39. Ali, A.; Chiang, Y.W.; Santos, R.M. X-ray Diffraction Techniques for Mineral Characterization: A Review for Engineers of the Fundamentals, Applications, and Research Directions. *Minerals* **2022**, *12*, 205. [CrossRef]
40. Mitra, P.; Chatterjee, A.; Maiti, H. ZnO thin film sensor. *Mater. Lett.* **1998**, *35*, 33–38. [CrossRef]
41. Riaz, M.; Fulati, A.; Zhao, Q.X.; Nur, O.; Willander, M.; Klason, P. Buckling and mechanical instability of ZnO nanorods grown on different substrates under uniaxial compression. *Nanotechnology* **2008**, *19*, 415708. [CrossRef]
42. Yang, W.; Liu, J.; Guan, Z.; Liu, Z.; Chen, B.; Zhao, L.; Li, Y.; Cao, X.; He, X.; Zhang, C.; et al. Morphology, electrical and optical properties of magnetron sputtered porous ZnO thin films on Si(100) and Si(111) substrates. *Ceram. Int.* **2020**, *46*, 6605–6611. [CrossRef]
43. Al-Gaashani, R.; Radiman, S.; Daud, A.; Tabet, N.; Al-Douri, Y. XPS and optical studies of different morphologies of ZnO nanostructures prepared by microwave methods. *Ceram. Int.* **2013**, *39*, 2283–2292. [CrossRef]
44. Karunakaran, C.; Gomathisankar, P.; Manikandan, G. Preparation and characterization of antimicrobial Ce-doped ZnO nanoparticles for photocatalytic detoxification of cyanide. *Mater. Chem. Phys.* **2010**, *123*, 585–594. [CrossRef]
45. Chen, Y.; Jyoti, N.; Hyun-U, K.; Kim, J. Effect of annealing temperature on the characteristics of ZnO thin films. *J. Phys. Chem. Solids* **2012**, *73*, 1259–1263. [CrossRef]
46. Abdullin, K.A.; Gabdullin, M.T.; Zhumagulov, S.K.; Ismailova, G.A.; Gritsenko, L.V.; Kedruk, Y.Y.; Mirzaeian, M. Stabilization of the Surface of ZnO Films and Elimination of the Aging Effect. *Materials* **2021**, *14*, 6535. [CrossRef]
47. Hsieh, P.-T.; Chen, Y.-C.; Kao, K.-S.; Wang, C.-M. Luminescence mechanism of ZnO thin film investigated by XPS measurement. *Appl. Phys. A* **2008**, *90*, 317–321. [CrossRef]
48. Cruz, M.A.; Ceballos-Sanchez, O.; Luévano-Hipólito, E.; Torres-Martínez, L. ZnO thin films deposited by RF magnetron sputtering: Effects of the annealing and atmosphere conditions on the photocatalytic hydrogen production. *Int. J. Hydrogen Energy* **2018**, *43*, 10301–10310. [CrossRef]

49. Lin, L.; Liu, J.; Lv, J.; Shen, S.; Wu, X.; Wu, D.; Qu, Y.; Zheng, W.; Lai, F. Correlation between native defects and morphological, structural and optical properties of ZnO nanostructures. *J. Alloys Compd.* **2017**, *695*, 1523–1527. [CrossRef]
50. Chen, K.; Zhu, H.; Yi, X.; Cheng, S.; Li, J.; Wang, S.; Lu, M.; Xu, M.; Ma, L.; Lv, L. Role of oxygen defects in inducing the blue photoluminescence of zinc oxide films deposited by magnetron sputtering. *Chin. Opt. Lett.* **2015**, *13*, 103101–103104. [CrossRef]
51. Das, D.; Mondal, P. Photoluminescence phenomena prevailing in c-axis oriented intrinsic ZnO thin films prepared by RF magnetron sputtering. *RSC Adv.* **2014**, *4*, 35735–35743. [CrossRef]
52. Damberga, D.; Viter, R.; Fedorenko, V.; Iatsunskyi, I.; Coy, E.; Graniel, O.; Balme, S.; Miele, P.; Bechelany, M. Photoluminescence Study of Defects in ZnO-Coated Polyacrylonitrile Nanofibers. *J. Phys. Chem. C* **2020**, *124*, 9434–9441. [CrossRef]
53. Al-Hashem, M.; Akbar, S.; Morris, P. Role of Oxygen Vacancies in Nanostructured Metal-Oxide Gas Sensors: A Review. *Sensors Actuators B Chem.* **2019**, *301*, 126845. [CrossRef]
54. Dellis, S.; Pliatsikas, N.; Kalfagiannis, N.; Lidor-Shalev, O.; Papaderakis, A.; Vourlias, G.; Sotiropoulos, S.; Koutsogeorgis, D.C.; Mastai, Y.; Patsalas, P. Broadband luminescence in defect-engineered electrochemically produced porous Si/ZnO nanostructures. *Sci. Rep.* **2018**, *8*, 6988. [CrossRef] [PubMed]
55. Kabir, A.; Bouanane, I.; Boulainine, D.; Zerkout, S.; Schmerber, G.; Boudjema, B. Photoluminescence Study of Deep Level Defects in ZnO Thin Films. *Silicon* **2019**, *11*, 837–842. [CrossRef]
56. Jazmati, A.K.; Abdallah, B. Optical and Structural Study of ZnO Thin Films Deposited by RF Magnetron Sputtering at Different Thicknesses: A Comparison with Single Crystal. *Mater. Res.* **2018**, *21*, 1–6. [CrossRef]
57. Kocsis, K.; Niedermaier, M.; Bernardi, J.; Berger, T.; Diwald, O. Changing interfaces: Photoluminescent ZnO nanoparticle powders in different aqueous environments. *Surf. Sci.* **2016**, *652*, 253–260. [CrossRef]
58. Gadallah, A.-S.; El-Nahass, M.M. Structural, Optical Constants and Photoluminescence of ZnO Thin Films Grown by Sol-Gel Spin Coating. *Adv. Condens. Matter Phys.* **2013**, *2013*, 234546. [CrossRef]
59. Galdámez-Martinez, A.; Santana, G.; Güell, F.; Martínez-Alanis, P.R.; Dutt, A. Photoluminescence of ZnO Nanowires: A Review. *Nanomaterials* **2020**, *10*, 857. [CrossRef]